Nanoscale

Accepted Manuscript

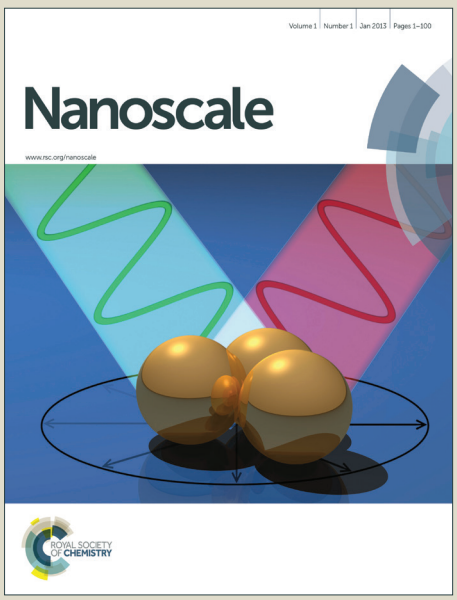

ROYAL SOCIETY OF CHEMISTRY

www.rsc.org/nanoscale

Nanoscale

RSCPublishing

ARTICLE

Porous Cobalt-Manganese Oxide Nanocubes Derived from Metal Organic Frameworks as Cathode Catalysts for Rechargeable Li-O_2 Batteries

Jian Zhang,[ab] Liangjun Wang,[c] Leilei Xu,[b] Xiaoming Ge,[d] Xiao Zhao,[b] Min Lai,[a] Zhaolin Liu,[d*] and Wei Chen[bce*]

Cite this: DOI: 10.1039/x0xx00000x

Received 00th January 2012,
Accepted 00th January 2012

DOI: 10.1039/x0xx00000x

www.rsc.org/

Developing cathode catalysts with porous structure is essential to design Li-O_2 battery with high rate performance and good cycle stability. Herein, spinel-type porous cobalt-manganese oxide (Co-Mn-O) nanocubes derived from metal organic frameworks were employed as electrocatalyst in Li-O_2 battery. The battery with porous Co-Mn-O nanocubes electrode shows low overpotential and enhanced capacity. The synergistic effects of large specific surface area, porous structure, and high electrocatalytic activity of porous Co-Mn-O nanocubes electrode ensure the Li-O_2 battery with good rate performance and excellent cycle stability up to 100 cycles.

Introduction

Recently, fast-growing market of hybrid vehicles has led to increasing demands for ultra-high-energy-density storage systems.[1] Rechargeable Li-O_2 battery with remarkably high theoretical energy density has attracted extensive attention.[2, 3] The theoretical energy density of the Li-O_2 battery is around 10 times higher than that of the current Li-ion battery, due to that the cathode active material (oxygen) can be obtained directly from the environment and no need to be stored in the battery.[4, 5] However, Li-O_2 battery suffers many challenges for practical applications, such as high overpotential, low rate capacity and poor cycle stability.[3, 6-8] The key factor to tackle these issues is to develop highly-efficient cathode catalysts, which can promote the oxygen reduction reaction (ORR) and oxygen evolution reaction (OER), thereby leading to a reduced overpotential and an enhanced cycle performance.[9-17] It has been reported that the cycle stability and rate performance were also dramatically affected by cathode passivation,[18, 19] because of the unavoidable formation of side products (Li_2CO_3 et al.) in the discharge-charge process. These side products are indecomposable and could continuously accumulate on the cathode to cover the catalytic active sites of the catalyst, to clog the pores of the air cathode and to block the pathways of oxygen and electrolyte, thereby resulting in cathode passivation and battery death.[20-23] Many studies have suggested that the presence of mesoporous structure can facilitate the transportation of oxygen and electrolyte, as well as minimize the undesirable clogging of the air cathode. [5, 19, 24-27] In addition, catalysts with porous structure usually possess large surface area and can provide more catalytic active sites to promote the ORR/OER. Therefore, our motivation is to develop cathode catalysts with desired porous structure that can improve the rate performance and cycle stability of the Li-O_2 battery.

Spinel oxides (AB_2O_4), which have been widely used as electrode materials in Li-ion batteries[28, 29], zinc-air batteries[30, 31] and supercapacitors[32, 33] Recently they have also been demonstrated as efficient catalysts for Li-O_2 batteries.[6, 34-37] R. Black and co-workers synthesized Co_3O_4 on reduced graphene oxide as electrocatalyst for Li-O_2 battery, exhibiting a low overpotential of 3.65 V.[11] Ma and his colleagues have developed multiporous $MnCo_2O_4$ microspheres as an efficient bi-functional catalyst for non-aqueous Li-O_2 batteries and cycled the battery for 50 cycles.[38] Recently, nanoscale metal-organic frameworks (MOFs) with controlled structure have been recognized as promising precursors to synthesize porous spinel oxides.[39-42] For example, prussian blue analogue $Fe_3[Co(CN)_6]_2 \cdot nH_2O$ nanoparticles have been used as sacrificial templates to prepare porous $Fe_xCo_{3-x}O_4$ nanosphere.[43] Chen and his group successfully synthesized porous Co_3O_4 nanocages by using MOFs nanocage as the starting precursors.[42] The metal oxides derived from metal-organic frameworks exhibit large surface area, uniform inter-connected pore structure and hierarchical pore size.[44, 45] All of these features are crucial for the cathode catalyst design for Li-O_2 battery.

In present study, porous spinel-type cobalt-manganese oxide (Co-Mn-O) nanocubes derived from MOFs were synthesized and employed as cathode catalysts for Li-O_2 battery. The as-prepared catalyst showed high catalytic activity towards both ORR and OER with reduced overpotentials. The battery assembled with the porous Co-Mn-O nanocubes electrode showed enhanced specific capacity and rate performance. Improved cycle stability up to 100 cycles was also obtained with a limited capacity of 500 mAh g^{-1}.

Experiments

Synthesis of Co-Mn-O

The nanocube-like MOF precursors were synthesized via modified self-assembly methods[46, 47]. Typically, 0.0372g $Mn(CH_3COO)_2 \cdot 4H_2O$ and 0.6g polyvinyl pyrrolidone (PVP) were dissolved in 7 ml deionized (DI) water and 30 ml absolute ethanol to form a transparent solution. 20 ml 0.04 mmol $K_3[Co(CN)_6]_2$ was then added dropwise into the above solution by using a syringe. The mixed solution was kept under room temperature for 24h. The resulting white precipitate was collected and washed several times with absolute ethanol, finally dried in an oven at 80℃. After that, the precursors were annealed at 475℃ for 1.5 h in air to obtain the finial products.

Characterization

Scanning electron microscope (SEM) images were collected on JEOL JSM 6700F and transmission electron microscope (TEM) experiments were conducted on a JEOL 2010 microscope. X-ray diffraction (XRD) patterns were recorded from a PANalytical Empyren DY 708 diffractometer with Cu radiation (Cu Kα=0.15406 nm). The Rietveld refinement of the XRD pattern was implemented in TOPAS V3 software. Fourier transform-infrared (FT-IR) was carried out on FT-IR Spectrum 2000 (PerkinElmer). Brunauer-Emmett-Teller (BET) surface area was measured by nitrogen sorption at 77 K on a surface area & pore size analyzer (NOVA 2200e). Thermogravimetric Analysis (TGA) was performed by using TA instrument 2960 under air gas flow at 10 ℃ min^{-1} in the temperature range 30-800℃. The contents of the metal elements were determined by Dual-view Optima 5300 DV inductively coupled plasma-optical emission spectroscopy (ICP-OES) system.

Li-O_2 cell assembly

The air cathodes were fabricated by coating the catalyst slurry on carbon paper homogenously. Generally, the slurry was prepared by mixing 40% catalysts with 50% Vulcan XC-72 (VX-72) carbon (Cabot Carbon Ltd) and 10% polyvinylidene fluoride (PVDF), or 90% VX-72 carbon with 10% PVDF. The mass loading of the slurry on the electrode was about 1 mg cm^{-2}, and the discharge capacity was calculated based on the total weight of the electrode. Galvanostatic discharge-charge test of the Li-O_2 battery was carried out on LAND multi-channel battery testing system by using coin cells (Fig. S1) within a voltage window of 2.0-4.5 V (vs. Li/Li^+). All the coin cells were assembled in glove box under Argon atmosphere by using glass fiber membranes as the separator. 1 M lithium trifluoromethanesulfonate/tetraethylene glycol dimethyl ether ($LiCF_3SO_3$/TEGDME) was used as the electrolyte.

Results and Discussion

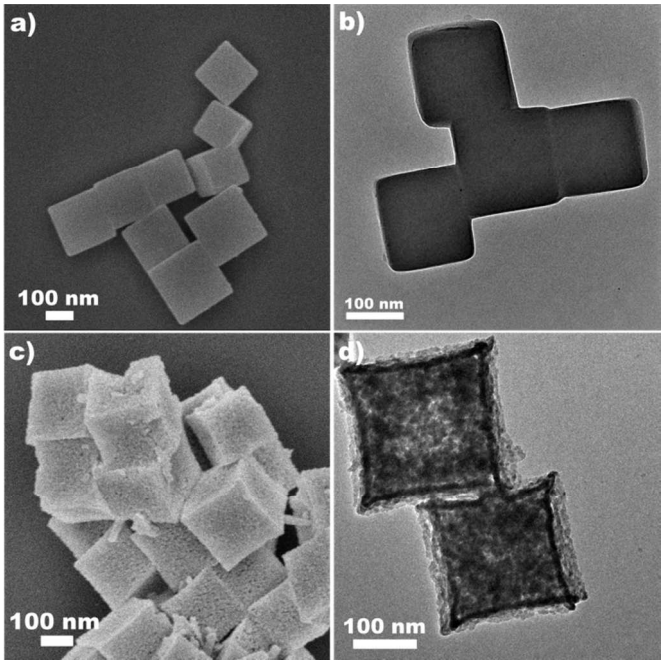

Fig. 1 SEM (a, c) and TEM (b, d) images of the obtained nanocube-like precursors before (a, b) and after (c, d) annealing, respectively.

The morphologies of the as-synthesized precursors and annealed products examined by SEM and TEM were shown in Fig. 1. Uniform nanocubic precursors with average size of 150-200 nm were obtained via the facile solution method. The nanocubic precursors showed well-defined cubic shape and smooth facets (Fig. 1a and 1b). The formation of the cubic structure was due to the lower surface energy of {100} facets in fcc nanocrystal.[48] When the cubic grows, ions tend to attach along {100} facets to minimize the surface energy.[47] The good uniformity in size and shape of the as-synthesized precursor was attributed to the use of ethanol and PVP, which can slow down the self-assembly process and prevent the particles agglomeration, respectively.[46, 47] The XRD pattern (Fig. S2) demonstrated that these precursors were $Mn_3[Co(CN)_6]_2 \cdot 9H_2O$ (PDF#51-1989). After annealing, the surface of the precursors became rough and porous structure was formed (Fig 1c and 1d). There was negligible change in the shape and size of the annealed products, indicating the good structural stability of the precursors. The ICP analysis indicated that the annealed products comprised 12.7 wt % Co and 16.7 wt % Mn, reflecting the Co/Mn mole ratio equalled to 2/3, which was consistent with that in the MOF precursors. The crystallographic structure and phase composition of the annealed products were determined by XRD. Two sets of diffraction peaks index to tetragonal $(Co,Mn)(Co,Mn)_2O_4$ phase

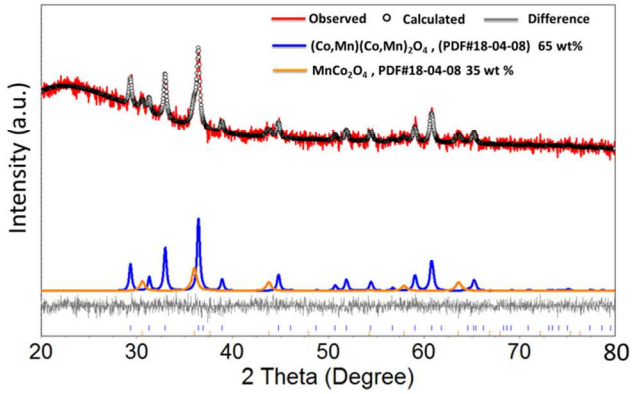

Fig. 2 XRD pattern of the nanocube-like precursors after annealing.

(I41/amdS; PDF#18-0408) and cubic $MnCo_2O_4$ phase (Fd-3m; PDF#23-1237) were observed in Fig.2. The Rietveld refinement of the XRD pattern indicated that the mass fraction of tetragonal $(Co,Mn)(Co,Mn)_2O_4$ and cubic $MnCo_2O_4$ were 65 wt % and 35 wt %, respectively. The $(Co,Mn)(Co,Mn)_2O_4$ was an intermediate spinel structure between the normal spinel structure (AB_2O_4) and inverse spinel structure ($B[AB]O_4$), with the formula of $(A_{1-x}B_x)(A_{x/2}B_{1-x/2})_2O_4$. Due to the similar chemical states and ionic radius, Co and Mn cations were miscible and tended to randomly scatter in the octahedral and tetrahedral sites of the $(Co,Mn)(Co,Mn)_2O_4$ phase. The mole ratio of Co/Mn in the $(Co,Mn)(Co,Mn)_2O_4$ component was about 0.77/2.23.

In addition, clear lattice spacing of 0.487 nm and 0.271 nm were observed in the high-resolution TEM image (Fig. 3c), in good agreement with the inter-plane spacing of spinel-type $(Co,Mn)(Co,Mn)_2O_4$ (111) and (113) planes, respectively. The slective area electron diffraction (SAED) pattern (Fig. 3c inset) showed that the annealed products were polycrystalline. The element mapping was carried out to illustrate the spatial distribution of Co, Mn and O species in the polycrystalline nanacubes (Fig. 3d, 3e and 3f). It revealved that the Co, Mn and O were homogeously distributed in the porous Co-Mn-O nanocubes.

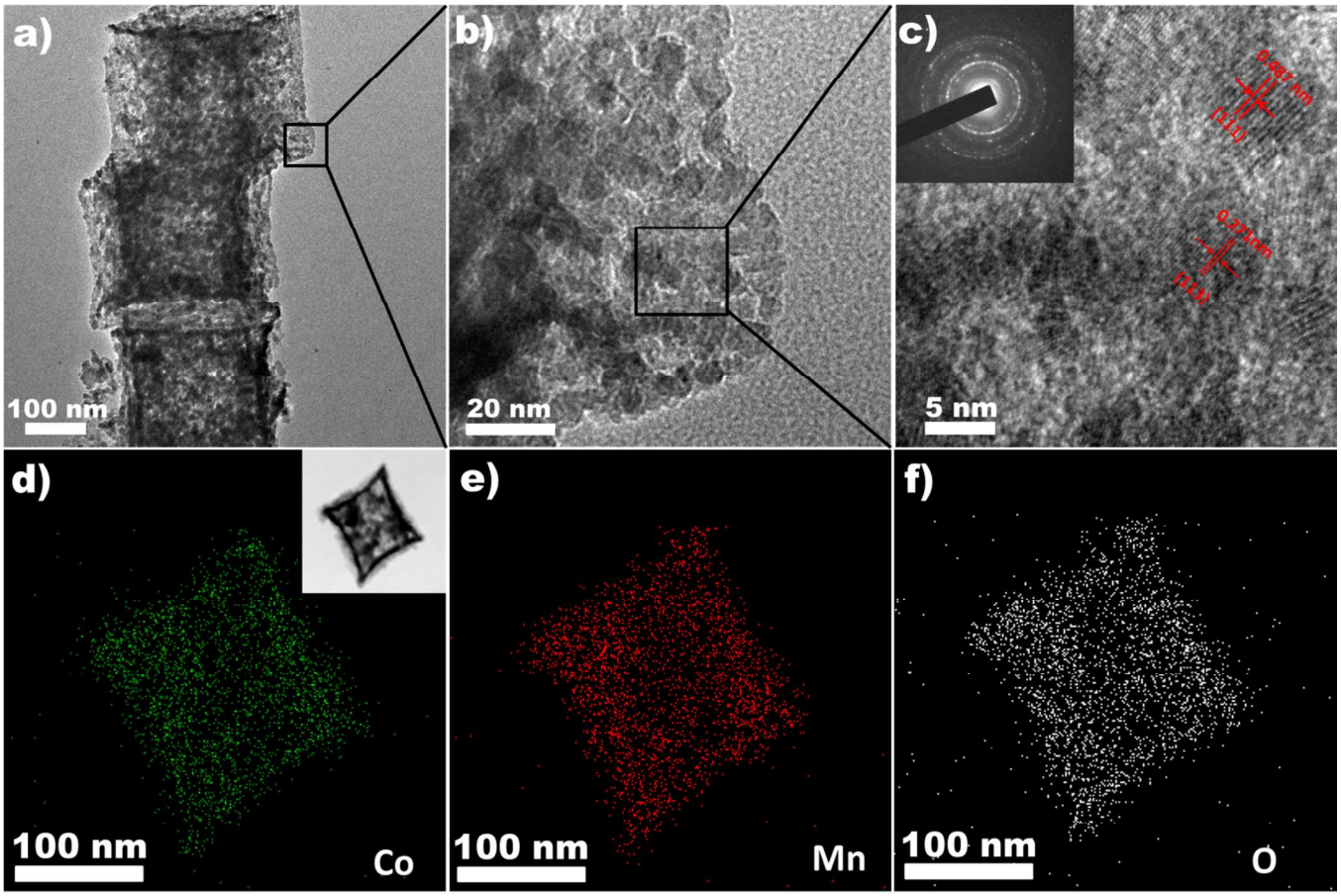

Fig. 3 HR-TEM images (a, b, c) and SAED pattern (c inset) of porous Co-Mn-O nanocubes; EDX mapping (d, e, f) of porous Co-Mn-O nanocubes.

The porosity of the annealed products was determined by N_2 adsorption-desorption measurement. The Nitrogen adsorption-desorption isotherms were displayed in Fig. 4a. It could be observed that the isotherm was type IV with H3-shaped hysteresis loops, which was the typical characteristics for the presence of mesopores. The pore volume the annealed products is about 0.22 $cm^3 g^{-1}$. These pores refer to the interspace between the aggregated nanoparticles in the nanocubes. The BET specific surface area of the porous Co-Mn-

O nanocubes was up to 110 m^2 g^{-1} (Fig. 4a), which is much higher than those of the reported spinel-type oxides catalysts.[28, 36, 49, 50] The pore size distribution of the annealed products calculated from the Barrett–Joyner–Halenda (BJH) method was shown as inset of Fig. 4a. A bimodal pore distribution centered at about 4 nm and 6 nm was observed. The porosity was generated from the release of gas molecules during the calcination of the MOF precursors.[39] The decomposition behavior of the nanocubic precursors during the calcination was investigated by thermogravimetric analysis (TGA). A significtant weight loss about 31 wt% was observed between 300℃ and 365℃ (Fig. S3) due to the oxidation of the cyanide and residual PVP. This result was also evidenced by the FT-IR spectrum

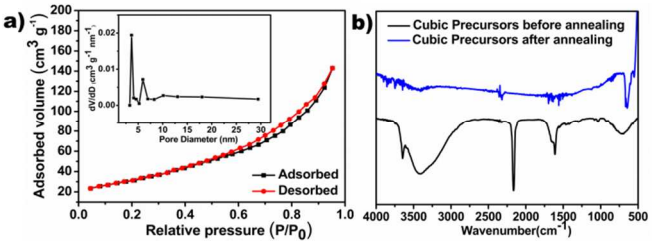

Fig. 4 (a) Nitrogen adsorption-desorption isotherms and pore size distribution (inset) of porous Co-Mn-O nanocubes catalyst; (b) FT-IR spectrum of the MOF precursor before (black) and after (blue) annealing.

in Fig 4b. The dominant peaks at 2170 cm^{-1} attributed to CN stretching and 1640 cm^{-1} for the C=O stretching of the PVP amide unit disappeared after annealing. The variation of the spectra suggested that C and N atoms were oxided into gases and escaped, thus giving rise to the formation of inter-connected small pores.[39] The formation of inter-connected pores can generate a 3D structure of the nanocubes and expose more active catalytic sites. These inter-connected pores can also facilitate the diffusion of oxygen and electrolyte. All of these factors can improve the performance of Li-O_2 battery.

The battery performance of the porous Co-Mn-O nanocubes catalyst was characterized by the galvanostatic charge-discharge test in coin cells. Due to the relative poor electrical conductivity of metal oxide, VX-72 carbon black was used as the electrically conductive additive, mixed with Co-Mn-O nanocubes catatlyst to form a conducting matrix as the air cathode. Fig. 5a shows the first discharge-charge profiles of the Li-O_2 cells with porous Co-Mn-O nanocubes and VX-72 carbon electrodes at a current density of 0.04 mA cm^{-2}. The open circuit voltages of these two batteries were all about 3.1-3.2 V. It can be seen that the porous Co-Mn-O nanocubes presented an improved ORR and OER activity with reduced voltage gap, which was about 200 mV lower than that of VX-72 carbon electrode. The round-trip efficiency (the ratio of discharge to charge voltage) of the Li-O_2 cell with porous Co-Mn-O nanocubes electrode was about 68%, which was higher than that of VX-72 carbon electrode (63%). Enhanced capacity of the battery cell with porous Co-Mn-O nanocubes electrode was also observed in Fig. 5a. The first discharge capacity of the battery cell with porous Co-Mn-O nanocubes electrode was up to 7653 mAh g^{-1}, which was

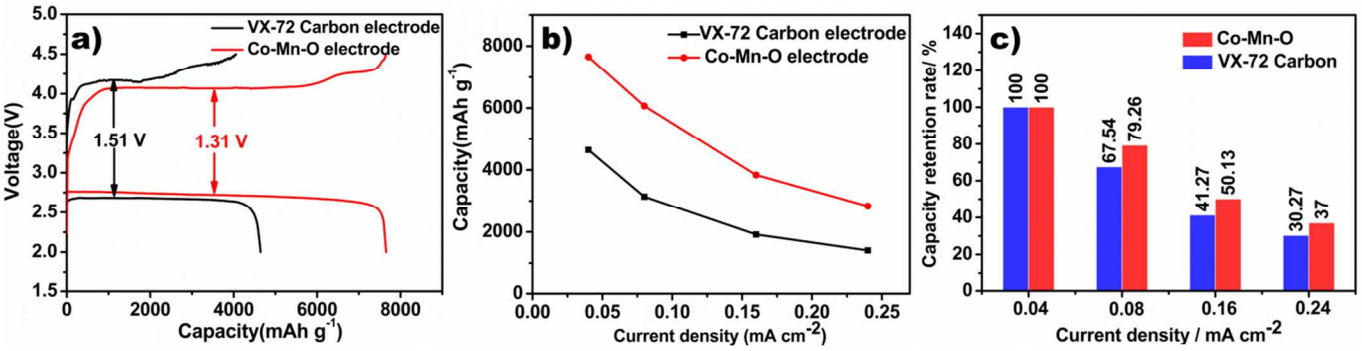

Fig. 5 (a) First discharge-charge curves of Li-O_2 batteries with porous Co-Mn-O nanocubes and VX-72 carbon electrodes at 0.04 mA cm^{-2}; (b) Discharge capacity and (c) capacity retention capacity of Li-O_2 battery cells with different electrode at various current density.

significantly higher than that of the VX-72 carbon electrodes (4644 mAh g^{-1}). This value was also higher than that of the catalysts with the similar composition.[38, 51, 52] The enhanced capacity of the porous Co-Mn-O nanocubes electrode was attributed to its higher catalytic activity to promote the ORR. Their large surface area also offered sufficient active sites to catalyze the ORR. We further conducted the battery tests at different current densities to explore the rate performance of the Li-O_2 battery (Fig. S4). It can be seen that the batteries with the porous Co-Mn-O nanocubes electrodes showed both higher discharge capacity (Fig. 5b) and higher capacity retention (Fig. 5c) under all current densities. The improved rate performance of porous Co-Mn-O electrode was ascribed to the porous structure, which could ensure the fast transportation of oxygen and electrolyte, and hence promote the mass transfer during the formation and decomposition of Li_2O_2.

The full capacity discharge-charge cycle performance of the Li-O_2 battery was examined at the current density of 0.16mA cm^{-2} (Fig. 6). As shown in Fig. 6a, the carbon electrode delivered reasonable high capacity at the first discharge process, however only 30% of the capacity was recharged during the charge process. The average coulombic efficiency of the VX-72 carbon electrode was only 50% during the first 5 cycles (Fig. 6c). The poor charging efficiency of VX-72 carbon electrode resulted in the incomplete decomposition of the discharge

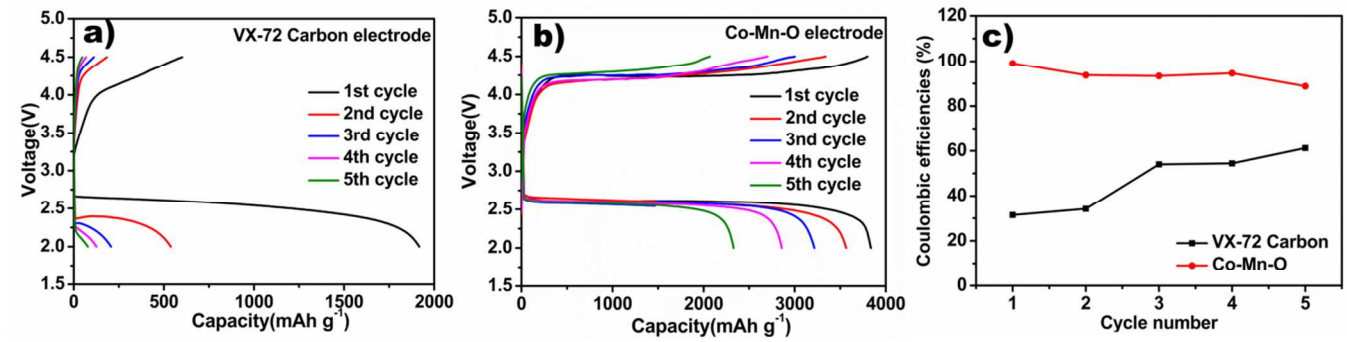

Fig. 6 Discharge-charge curves of Li-O_2 batteries with VX-72 carbon (a) and porous Co-Mn-O nanocubes (b) electrodes at 0.16 mA cm^{-2}; (c) Comparison of coulombic efficiency of Li-O_2 batteries with different electrodes.

products, and aggravated the resistance and passivation of the air cathode.[19] Therefore, rapid capacity decay was observed and less than 10% capacity was retained after 5 discharge-charge cycles (Fig. 6a). In contrast, most of the discharge capacity of the Li-O_2 cell with porous Co-Mn-O nanocubes electrode was re-charged on each cycle. The average coulombic efficiency was up to 95% (Fig. 6c). In this case, 54% capacity was kept of the Li-O_2 cell with porous Co-Mn-O nanocubes electrode after 5 discharge-charge cycles. These results emphasized that the porous Co-Mn-O nanocubes catalysts can improve the charge efficiency effectively, thus ensured the recovery of the electrode porosity during the charge process and resulted in enhanced cycle performance of the battery.

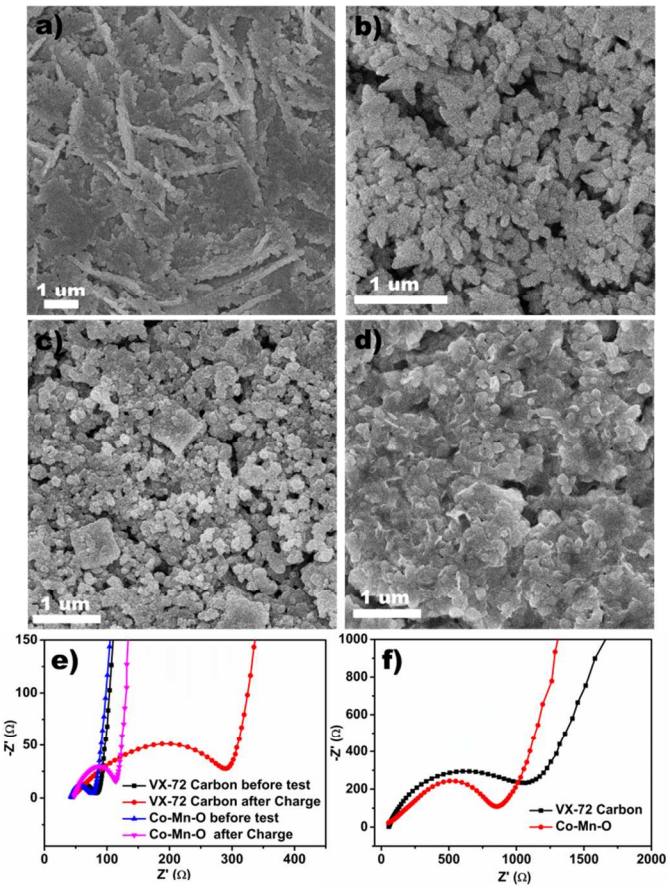

Fig. 7 SEM images of the porous Co-Mn-O nanocubes electrode (a, c) and VX-72 carbon electrode (b, d) after 1st discharge (a, b) and after 1st charge (c, d); (e), (f) Electrochemical impedance spectra of Li-O_2 batteries with VX-72 carbon and porous Co-Mn-O nanocubes electrodes at different discharge-charge state.

The SEM and electrochemical impedance spectra (EIS) measurements of the batteries at different test states were conducted to further verify the high charge efficiency of Co-Mn-O electrode. Fig. 7a-d shows the SEM images of the porous Co-Mn-O nanocubes and VX-72 carbon electrodes at different discharge-charge states. The discharge products Li_2O_2 evidenced by XRD (Fig. S5) were deposited on the surface of these two electrodes (Fig. 7a and 7b) after first discharge process. After charge process, the discharge products on porous Co-Mn-O nanocubes electrode were decomposed completely (Fig. 7c); while parts of the discharge products coating on the VX-72 carbon electrode were still remained (Fig. 7d). These results indicated that the porous Co-Mn-O nanocubes electrodes had higher OER activity and charge efficiency than that of the VX-72 carbon electrode. In addition, similar trends were also observed during the EIS measurement. As shown in Fig. 7g, the battery cells with VX-72 carbon and porous Co-Mn-O nanocubes electrodes showed almost the same impedance before test (Fig. 7e). The impedance of both cells increased significantly after first discharge process (Fig.7f), which is mainly due to the deposition of insulated discharge products Li_2O_2. After charging, the impedance of the battery with porous Co-Mn-O nanocubes electrode was nearly recovered due to the fully decomposition of Li_2O_2 (Fig. 7e). However, the impedance of the cell with VX-72 carbon electrode was still as high as 300 Ω (Fig.7e), indicating the incomplete decomposition of the Li_2O_2 [24].

The long cycle stability of the porous Co-Mn-O nanocubes electrode was measured following a widely adopted method[26, 53, 54] by limiting the discharge capacity to 500 mAh g^{-1}. Fig. 8a and 8c are the voltage profiles of the batteries with porous Co-Mn-O nanocubes and VX-72 carbon electrodes cycled at the current density of 0.16 mA cm^{-2}. It can be seen that the battery

with porous Co-Mn-O nanocubes electrode can run 100 cycles without any obvious discharge capacity fading (Fig. 8b), while the cycle numbers were limited to 29 for VX-72 carbon electrode (Fig. 8d). To our knowledge this was one of the best cycle performances among the reported catalysts with similar compositions.[38, 51, 52] These results further highlight that the porous Co-Mn-O nanocubes electrode has excellent long cycle stability.

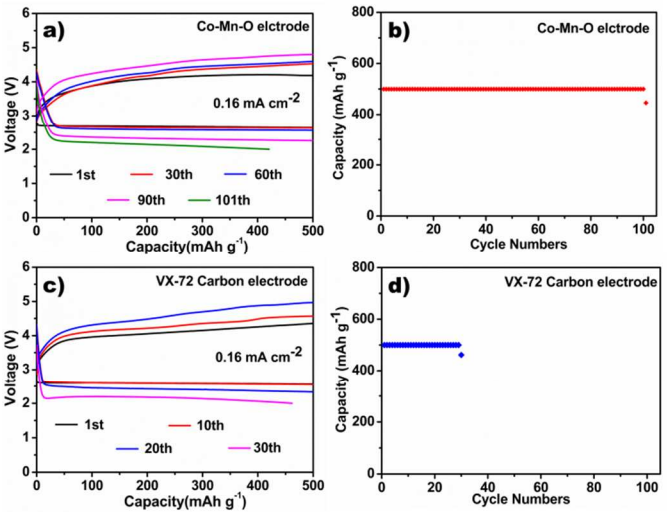

Fig. 8 Cyclic performance of (a, b) porous Co-Mn-O nanocube electrode and (c, d) VX-72 carbon electrode at 0.16 mA cm^{-2}; (a, c) Discharge/charge curves at different cycles; (b, d) capacity of discharge vs. cycle number.

Conclusions

In summary, porous Co-Mn-O nanocubes with large specific surface area were synthesized and employed as cathode catalyst for Li-O_2 battery. The catalyst showed good ORR and OER catalytic activity with considerable reduced overpotentials (200 mV) during the discharge-charge process. The battery assembled with porous Co-Mn-O nanocubes also possessed enhanced specific capacity and improved rate performance. Excellent cycle stability up to 100 cycles was also obtained by using the porous Co-Mn-O nanocubes electrode. The enhanced battery performance can be ascribed to the synergistic effect of both the high catalytic activity and the porous structure of spinel-type cobalt-manganese oxide.

Acknowledgements
The authors acknowledge the financial support from the Singapore MOE grants R143-000-530-112 and 2014-T2-1-038.

Notes and references

[a] School of Physics and Optoelectronic Engineering, Nanjing University of Information Science & Technology, Nanjing 210044, Jiangsu, China
[b] Department of Chemistry, National University of Singapore, 3 Science Drive 3, 117543, Singapore
[c] Department of Physics,National University of Singapore, 2 Science Drive 3, 117543Singapore
[d] Institute of Materials Research and Engineering (IMRE), Agency of Science, Technology, and Research (A*STAR), 3 Research Link, Singapore 117602, Singapore.
[e] National University of Singapore (Suzhou) Research Institute, Suzhou, China

*Corresponding authors
Prof. Dr. Chen Wei,
Tel: 65-6516 2921. Fax: 65-6777 6126. E-mail: phycw@nus.edu.sg

Dr. Liu Zhaolin, E-mail: zl-liu@imre.a-star.edu.sg

Electronic Supplementary Information (ESI) available: [details of any supplementary information available should be included here]. See DOI: 10.1039/b000000x/

Reference

1. P. G. Bruce, S. A. Freunberger, L. J. Hardwick and J.-M. Tarascon, *Nat. Mater.*, 2012, **11**, 19-29.
2. R. Cao, J. S. Lee, M. L. Liu and J. Cho, *Adv. Energy Mater.*, 2012, **2**, 816-829.
3. A. Kraytsberg and Y. Ein-Eli, *J. Power Sources*, 2011, **196**, 886-893.
4. Y. Zhao, L. Xu, L. Mai, C. Han, Q. An, X. Xu, X. Liu and Q. Zhang, *Proc. Natl. Acad. Sci.*, 2012, **109**, 19569-19574.
5. J.-J. Xu, Z.-L. Wang, D. Xu, L.-L. Zhang and X.-B. Zhang, *Nat Commun*, 2013, **4**.
6. Y. Shao, S. Park, J. Xiao, J.-G. Zhang, Y. Wang and J. Liu, *ACS Catal.*, 2012, **2**, 844-857.
7. G. Girishkumar, B. McCloskey, A. C. Luntz, S. Swanson and W. Wilcke, *J. Phys. Chem. Lett.*, 2010, **1**, 2193-2203.
8. F. Li, T. Zhang and H. Zhou, *Energy Environ. Sci.*, 2013, **6**, 1125-1141.
9. F. Li, Y. Chen, D.-M. Tang, L. Z. Jian, C. Liu, D. Golberg, A. Yamada and H. Zhou, *Energy Environ. Sci.*, 2014.
10. F. Li, D.-M. Tang, Y. Chen, D. Golberg, H. Kitaura, T. Zhang, A. Yamada and H. Zhou, *Nano Lett.*, 2013, **13**, 4702-4707.
11. R. Black, J.-H. Lee, B. Adams, C. A. Mims and L. F. Nazar, *Angew. Chem. Int. Ed.*, 2013, **52**, 392-396.
12. K.-N. Jung, J.-I. Lee, W. B. Im, S. Yoon, K.-H. Shin and J.-W. Lee, *Chem. Commun.*, 2012, **48**, 9406-9408.
13. E. Yilmaz, C. Yogi, K. Yamanaka, T. Ohta and H. R. Byon, *Nano Lett.*, 2013, **13**, 4679-4684.
14. W. Zhang, J. Zhu, H. Ang, Y. Zeng, N. Xiao, Y. Gao, W. Liu, H. H. Hng and Q. Yan, *Nanoscale*, 2013, **5**, 9651-9658.
15. J. Li, H. Zhang, Y. Zhang, M. Wang, F. Zhang and H. Nie, *Nanoscale*, 2013, **5**, 4647-4651.
16. X. Hu, X. Han, Y. Hu, F. Cheng and J. Chen, *Nanoscale*, 2014, **6**, 3522-3525.

17. J. Zhang, Y. Zhao, X. Zhao, Z. Liu and W. Chen, *Sci. Rep.*, 2014, **4**.
18. Y. Qin, J. Lu, P. Du, Z. Chen, Y. Ren, T. Wu, J. T. Miller, J. Wen, D. J. Miller, Z. Zhang and K. Amine, *Energy Environ. Sci.*, 2013, **6**, 519.
19. H. D. Lim, K. Y. Park, H. Song, E. Y. Jang, H. Gwon, J. Kim, Y. H. Kim, M. D. Lima, R. Ovalle Robles, X. Lepro, R. H. Baughman and K. Kang, *Adv Mater*, 2013, **25**, 1348-1352.
20. B. D. McCloskey, A. Speidel, R. Scheffler, D. C. Miller, V. Viswanathan, J. S. Hummelshøj, J. K. Nørskov and A. C. Luntz, *J. Phys. Chem. Lett.*, 2012, **3**, 997-1001.
21. M. M. Ottakam Thotiyl, S. A. Freunberger, Z. Peng and P. G. Bruce, *J. Am. Chem. Soc.*, 2012, **135**, 494-500.
22. W. Xu, J. Hu, M. H. Engelhard, S. A. Towne, J. S. Hardy, J. Xiao, J. Feng, M. Y. Hu, J. Zhang, F. Ding, M. E. Gross and J.-G. Zhang, *J. Power Sources*, 2012, **215**, 240-247.
23. B. M. Gallant, R. R. Mitchell, D. G. Kwabi, J. Zhou, L. Zuin, C. V. Thompson and Y. Shao-Horn, *J. Phys. Chem. C*, 2012, **116**, 20800-20805.
24. X. Zhang, j.-J. Xu, Z. Wang, D. Xu and H. Wang, *Energy Environ. Sci.*, 2013.
25. H.-D. Lim, H. Song, H. Gwon, K.-Y. Park, J. Kim, Y. Bae, H. Kim, S.-K. Jung, T. Kim, Y. H. Kim, X. Lepro, R. Ovalle-Robles, R. H. Baughman and K. Kang, *Energy Environ. Sci.*, 2013.
26. J.-J. Xu, D. Xu, Z.-L. Wang, H.-G. Wang, L.-L. Zhang and X.-B. Zhang, *Angew. Chem. Int. Ed.*, 2013, **52**, 3887-3890.
27. T.-F. Hung, S. G. Mohamed, C.-C. Shen, Y.-Q. Tsai, W.-S. Chang and R.-S. Liu, *Nanoscale*, 2013, **5**, 12115-12119.
28. L. Zhou, D. Zhao and X. W. Lou, *Advanced Materials*, 2012, **24**, 745-748.
29. L. Tao, J. Zai, K. Wang, H. Zhang, M. Xu, J. Shen, Y. Su and X. Qian, *J. Power Sources*, 2012, **202**, 230-235.
30. M. Prabu, P. Ramakrishnan and S. Shanmugam, *Electrochem. Commun.*, 2014, **41**, 59-63.
31. M. Prabu, P. Ramakrishnan, H. Nara, T. Momma, T. Osaka and S. Shanmugam, *ACS applied materials & interfaces*, 2014.
32. Q. Wang, X. Wang, B. Liu, G. Yu, X. Hou, D. Chen and G. Shen, *Journal of Materials Chemistry A*, 2013, **1**, 2468-2473.
33. X.-h. Xia, J.-p. Tu, Y.-j. Mai, X.-l. Wang, C.-d. Gu and X.-b. Zhao, *J. Mater. Chem.*, 2011, **21**, 9319-9325.
34. Y. Cui, Z. Wen and Y. Liu, *Energy Environ. Sci.*, 2011, **4**, 4727-4734.
35. F. Cheng and J. Chen, *Chem. Soc. Rev.*, 2012, **41**, 2172-2192.
36. L. Zhang, S. Zhang, K. Zhang, G. Xu, X. He, S. Dong, Z. Liu, C. Huang, L. Gu and G. Cui, *Chem. Commun.*, 2013, **49**, 3540-3542.
37. X. Lin, Y. Shang, T. Huang and A. Yu, *Nanoscale*, 2014, **6**, 9043-9049.
38. S. Ma, L. Sun, L. Cong, X. Gao, C. Yao, X. Guo, L. Tai, P. Mei, Y. Zeng, H. Xie and R. Wang, *The Journal of Physical Chemistry C*, 2013.
39. L. Hu and Q. Chen, *Nanoscale*, 2014, **6**, 1236-1257.
40. L. Zhang, H. B. Wu and X. W. Lou, *J. Am. Chem. Soc.*, 2013, **135**, 10664-10672.
41. L. Zhang, H. B. Wu, R. Xu and X. W. Lou, *CrystEngComm*, 2013, **15**, 9332-9335.
42. L. Hu, N. Yan, Q. Chen, P. Zhang, H. Zhong, X. Zheng, Y. Li and X. Hu, *Chemistry – A European Journal*, 2012, **18**, 8971-8977.
43. L. Hu, Y. Huang and Q. Chen, *J. Alloys Compd.*, 2013, **559**, 57-63.
44. L. Hu, P. Zhang, H. Zhong, X. Zheng, N. Yan and Q. Chen, *Chemistry – A European Journal*, 2012, **18**, 15049-15056.
45. L. Zhang, L. Shi, L. Huang, J. Zhang, R. Gao and D. Zhang, *ACS Catal.*, 2014, 1753-1763.
46. L. Hu, J.-y. Mei, Q.-w. Chen, P. Zhang and N. Yan, *Nanoscale*, 2011, **3**, 4270-4274.
47. L. Hu, P. Zhang, Q.-w. Chen, N. Yan and J.-y. Mei, *Dalton Trans.*, 2011, **40**, 5557-5562.
48. W. Lu, J. Fang, K. L. Stokes and J. Lin, *J. Am. Chem. Soc.*, 2004, **126**, 11798-11799.
49. W. Y. Li, L. N. Xu and J. Chen, *Adv. Funct. Mater.*, 2005, **15**, 851-857.
50. H. B. Wu, H. Pang and X. W. Lou, *Energy Environ. Sci.*, 2013, **6**, 3619-3626.
51. H. Wang, Y. Yang, Y. Liang, G. Zheng, Y. Li, Y. Cui and H. Dai, *Energy Environ. Sci.*, 2012, **5**, 7931-7935.
52. L. Wang, X. Zhao, Y. Lu, M. Xu, D. Zhang, R. S. Ruoff, K. J. Stevenson and J. B. Goodenough, *J. Electrochem. Soc.*, 2011, **158**, A1379-A1382.
53. D. Xu, Z.-l. Wang, J.-j. Xu, L.-l. Zhang and X.-b. Zhang, *Chem. Commun.*, 2012, **48**, 6948-6950.
54. Y. Chen, S. A. Freunberger, Z. Peng, O. Fontaine and P. G. Bruce, *Nat Chem*, 2013, **5**, 489-494.